ON THE IMPLEMENTATION OF ADVANCED TURBULENCE MODELS FOR UNSTRUCTURED-GRID AEROSPACE APPLICATIONS

Enda Dimitri Vieira Bigarella
Instituto Tecnológico de Aeronáutica, Centro Técnico Aeroespacial, São José dos Campos, SP, BRAZIL – 12228-900
enda.bigarella@ig.com.br

Farney Coutinho Moreira
Instituto de Aeronáutica e Espaço, Centro Técnico Aeroespacial, São José dos Campos, SP, BRAZIL – 12228-904
farney_moreira@yahoo.com

João Luiz F. Azevedo
Instituto de Aeronáutica e Espaço, Centro Técnico Aeroespacial, São José dos Campos, SP, BRAZIL – 12228-904
azevedo@iae.cta.br

Abstract. *Turbulent flow simulations are presented in this paper. A finite volume code for 3-D, unstructured, adaptive meshes to simulate turbulent flows is used. A fully explicit, 2nd-order accurate, 5-stage, Runge-Kutta time stepping scheme is used to perform the time march of the flow equations. Flux calculation on the volume faces is performed by a centred scheme which requires the addition of artificial dissipation terms. Boundary conditions are set using Riemann invariants. The implementation uses a cell centred, face-based data structure. In order to enhance the quality of the results, h-refinement routines are implemented in the code to adapt the original mesh. These routines are able to handle tetrahedra, hexahedra, triangular-base prisms and square-base pyramids. A sensor based on density gradients selects the elements to be refined. Simulations of turbulent flows over a flat plate are compared to theoretical results in order to assess the correctness of the implementation of the formulation. Transonic turbulent flows are, then, simulated about the Brazilian Satellite Launch Vehicle (VLS) configuration, currently under development at IAE. Two eddy viscosity turbulence models are chosen for this numerical method, considering single- and two-equation closures. The one-equation model implemented is the Spalart-Allmaras model whereas the two-equation closure is the Menter SST model. These two models were natively developed for aerospace applications. In general, good results within engineering error margins are obtained with the method presented here.*

Keywords: *Turbulence Models, CFD, Unstructured-Grid, Aerospace Configuration.*

1. Introduction

Many approaches have been developed to simulate aerodynamic flows over 3-D aerospace configurations within the CFD group at Instituto de Aeronáutica e Espaço (IAE). This paper discusses the results obtained using a finite volume method (FVM) on 3-D, unstructured, adaptive meshes to simulate inviscid and viscous flows over typical aerospace configurations.

The development in the computational resources available to IAE during the 90's made possible the simulation of axisymmetric turbulent flows (Zdravistch and Azevedo, 1990), and 3-D laminar viscous flows simulations could be performed with adequate mesh refinement (Azevedo *et al.*, 1996). Furthermore, axisymmetric meshes could be made refined enough to simulate complex turbulent flows and to capture the dependency of the formulation with the Reynolds number (Buonomo and Azevedo, 1997). The results presented in Bigarelli *et al.* (1999) showed the influence of the turbulence modelling in the flow configuration. The calculations emphasised that a laminar viscous formulation could not correctly capture some of the flow phenomena that might occur in the simulations of interest at IAE. Obviously, this is what one should expect since the Reynolds numbers of interest are of the order of $Re = 10^7$. Clearly, phenomena such as flow separation due to adverse pressure gradients and shock wave-boundary layer interactions are poorly represented by a laminar formulation at such high Reynolds numbers. Nevertheless, these phenomena play an important role in the flows over launch vehicles and, therefore, should be adequately simulated.

The present work is aimed at addressing the implementation and validation of turbulent closures for a finite volume computational tool under development at IAE. Hence, numerical results of the turbulent boundary layer over a flat plate are compared to known data in the literature in order to assess the correctness of the turbulent formulation added to the code. Furthermore, the computational code is used to simulate 3-D transonic and supersonic flows about the VLS and the hemisphere-cylinder configurations. The VLS is a four-stage satellite launcher built with four booster attached to a main body. Since experimental data is available for this configuration, the numerical results are compared with them such that the code effectiveness in the solution of realistic aerospace configuration flows can be assessed. In the present work, computations were performed

considering only the vehicle central body.

A fully explicit, 2nd-order accurate, 5-stage, Runge-Kutta time stepping scheme was used to perform the time march of the flow equations. For flux calculation on the volume faces, a centred scheme, which requires the addition of artificial dissipation terms, is used. The boundary conditions are set using Riemann invariants. The implementation uses a cell centred, face-based data structure and the code can use meshes with any combination of tetrahedra, hexahedra, triangular-base prisms and square-base pyramids.

2. Theoretical Formulation

The long term objective of the Computational Fluid Dynamics group at IAE is to develop the capability of simulating three-dimensional, viscous turbulent flows over general launch vehicle configurations. The present paper discusses the progress attained in the simulation of 3-D compressible viscous flows using a finite volume approach. Hence, the flows of interest in this present case are modelled by the compressible Reynolds-averaged Navier-Stokes equations. These equations can be written, considering the perfect gas assumption, as

$$\frac{\partial Q}{\partial t} + \frac{\partial E_e}{\partial x} + \frac{\partial F_e}{\partial y} + \frac{\partial G_e}{\partial z} = \frac{\partial E_v}{\partial x} + \frac{\partial F_v}{\partial y} + \frac{\partial G_v}{\partial z} \ , \tag{1}$$

where Q is the dimensionless vector of conserved variables, defined as

$$Q = \left[\begin{array}{cccccc} \rho & \rho\,u & \rho\,v & \rho\,w & e \end{array} \right]^T \ , \tag{2}$$

and ρ is the fluid density, u, v and w are the Cartesian velocity components and e is the fluid total energy per unit of volume. In this work, all the variables are nondimensionalised. The E_e, F_e and G_e terms are the dimensionless inviscid flux vectors and E_v, F_v and G_v are the dimensionless viscous flux vectors. The E_e, F_e and G_e vectors are given by

$$E_e = \left\{ \begin{array}{c} \rho\,u \\ \rho\,u^2 + p \\ \rho\,u\,v \\ \rho\,u\,w \\ (e+p)\,u \end{array} \right\} \ , \qquad F_e = \left\{ \begin{array}{c} \rho\,v \\ \rho\,v\,u \\ \rho\,v^2 + p \\ \rho\,v\,w \\ (e+p)\,v \end{array} \right\} \ , \qquad G_e = \left\{ \begin{array}{c} \rho\,w \\ \rho\,w\,u \\ \rho\,w\,v \\ \rho\,w^2 + p \\ (e+p)\,w \end{array} \right\} \ . \tag{3}$$

The viscous flux vectors can be written as

$$E_v = \frac{M_\infty}{Re} \left\{ \begin{array}{c} 0 \\ \tau_{xk} \\ \tau_{xk} \\ \tau_{xk} \\ \beta_x \end{array} \right\} \ , \qquad F_v = \frac{M_\infty}{Re} \left\{ \begin{array}{c} 0 \\ \tau_{yk} \\ \tau_{yk} \\ \tau_{yk} \\ \beta_y \end{array} \right\} \ , \qquad G_v = \frac{M_\infty}{Re} \left\{ \begin{array}{c} 0 \\ \tau_{zk} \\ \tau_{zk} \\ \tau_{zk} \\ \beta_z \end{array} \right\} \ , \tag{4}$$

where $k = x$, y or z. The viscous stress tensor is

$$\tau_{ij} = (\mu_\ell + \mu_t) \left[\left(\frac{\partial u_i}{\partial x_j} + \frac{\partial u_j}{\partial x_i} \right) - \frac{2}{3} \frac{\partial u_m}{\partial x_m} \delta_{ij} \right] \ , \tag{5}$$

and

$$\beta_i = \tau_{ij} u_j - q_i \ , \qquad q_j = \gamma \left(\frac{\mu_\ell}{Pr} + \frac{\mu_t}{Pr_t} \right) \frac{\partial e_i}{\partial x_j} \ , \tag{6}$$

where e_i is the dimensionless internal energy, defined as

$$e_i = \frac{T}{\gamma\,(\gamma - 1)} \ . \tag{7}$$

Furthermore, $Re = \rho_\infty \left| \vec{q}_\infty \right| \ell / \mu_\infty$ is the freestream Reynolds number, with $\left| \vec{q}_\infty \right|$ representing the magnitude of the freestream velocity. $M_\infty = \left| \vec{q}_\infty \right| / a_\infty$ is the freestream Mach number, Pr is the Prandtl number, which is assumed equal to 0.72, γ is the ratio of specific heats, μ is the molecular viscosity coefficient of the fluid, and ℓ is the characteristic length of the problem. The μ_t variable is the eddy viscosity coefficient, which is modelled by turbulence closures, and Pr_t is the turbulent Prandtl number, which is assumed equal to 0.9. In the previous equations, the dimensionless pressure, p, can be calculated from the perfect gas equation as

$$p = (\gamma - 1) \left[e - \frac{1}{2} \rho \left(u^2 + v^2 + w^2 \right) \right] \ . \tag{8}$$

One should observe that the Euler equations are formally obtained from the Navier-Stokes equations as Re approaches infinity.

The finite volume technique is used to obtain the solution of the Navier-Stokes equations. The formulation of the method is obtained by an integration of the flow equations in a finite volume. The application of Gauss theorem for each finite volume yields

$$\int_{V_i} \frac{\partial Q}{\partial t}\, dV + \int_{S_i} \left((E_e - E_v)\ \vec{i_x} + (F_e - F_v)\ \vec{i_y} + (G_e - G_v)\ \vec{i_z} \right) \cdot d\vec{S} = 0 \ , \tag{9}$$

where $d\vec{S}$ is the outward oriented normal area vector for the i-th control volume. The discrete value of the vector of conserved variables for the i-th control volume is defined as the mean value of the conserved variables in the volume, i.e.,

$$Q_i = \frac{1}{V_i} \int_{V_i} Q\, dV \ . \tag{10}$$

Hence, the final form of the finite volume formulation for the Navier-Stokes equations can be written for an elementary volume and assuming a stationary mesh as

$$\frac{\partial Q_i}{\partial t} = -\frac{1}{V_i} \sum_{k=1}^{nf} \left[(E_{ek} - E_{vk})\ \vec{i_x} + (F_{ek} - F_{vk})\ \vec{i_y} + (G_{ek} - G_{vk})\ \vec{i_z} \right] \cdot \vec{S}_k \ , \tag{11}$$

where nf is the number of faces which form the control volume and $\vec{S}_k$ is the outward oriented normal area vector of the k-th face. The code developed is able to simulate flows on grids comprised of tetrahedra, hexahedra, triangular-base prisms, square-base pyramids or a mix of these types of elements. The previous equation also indicates that the integral is discretized assuming the fluxes to be constant on the faces.

3. Numerical Formulation

3.1. Spatial Discretisation

The centred scheme used in this work for spatial discretisation was proposed by Jameson *et al.* (1981). For this scheme, the convective operator, $C(Q_i)$, is calculated as the sum of the inviscid fluxes on the faces of the i-th volume, i.e.,

$$C(Q_i) = \sum_{k=1}^{nf} \left[E_e(Q_k)\ \vec{i_x} + F_e(Q_k)\ \vec{i_y} + G_e(Q_k)\ \vec{i_z} \right] \cdot \vec{S}_k \ , \qquad Q_k = \frac{Q_m + Q_i}{2} \ . \tag{12}$$

In this expression, Q_m and Q_i are the conserved properties in the volumes at each side of the k-th face and m indicates the neighbour of the i-th element. The viscous operator in the i-th control volume, $V(Q_i)$, is calculated as the sum of the viscous fluxes on the faces which constitute the volume, i.e.,

$$V(Q_i) = \sum_{k=1}^{nf} \left[E_v(Q_k)\ \vec{i_x} + F_v(Q_k)\ \vec{i_y} + G_v(Q_k)\ \vec{i_z} \right] \cdot \vec{S}_k \ . \tag{13}$$

In this case, both the conserved variable vector and the derivatives on the face, used to compute the viscous terms, are calculated as the arithmetic average between these quantities in the two volumes which contain the face. Derivatives of flow variables, for each control volume, are calculated in the standard finite volume approach in which these derivatives are transformed, by the gradient theorem, into surface integrals around the control volume.

The artificial dissipation operator, $D(Q_i)$, is built by the undivided Laplacian and bi-harmonic operators. In regions of high property gradients, the bi-harmonic operator is turned off in order to avoid oscillations. In smooth regions, the undivided Laplacian operator is turned off in order to maintain 2nd order accuracy. A numerical pressure sensor is responsible for this switching between the operators. The expression for the artificial dissipation operator is given by

$$D(Q_i) = \sum_{m=1}^{nb} \left\{ \left(\frac{A_m + A_i}{2} \right) \left[\epsilon_2 (Q_m - Q_i) - \epsilon_4 \left(\nabla^2 Q_m - \nabla^2 Q_i \right) \right] \right\} \ , \tag{14}$$

where m represents the neighbours of the i-th element and nb is the total number of neighbours of the i-th control volume. The undivided harmonic operator can be written as

$$\nabla^2 Q_i = \sum_{m=1}^{nb} \left[Q_m - Q_i \right] \ . \tag{15}$$

The ϵ factors are based on the pressure sensor, where

$$\epsilon_2 = K_2 \max(\nu_i, \nu_m) \ , \qquad \epsilon_4 = \max(0, K_4 - \epsilon_2) \ , \qquad \nu_i = \frac{\sum_{m=1}^{nb} |p_m - p_i|}{\sum_{m=1}^{nb} [p_m + p_i]} \ . \tag{16}$$

In this work, K_2 and K_4 are assumed equal to 1/2 and 3/256, respectively. The A_i coefficients (Mavriplis, 1990) are calculated as described in the following expression.

$$A_i = \sum_{k=1}^{nf} \left[\left| \left(u_k \vec{i}_x + v_k \vec{i}_y + w_k \vec{i}_z \right) \cdot \vec{S}_k \right| + a_k \left| \vec{S}_k \right| \right] \ . \tag{17}$$

in an attempt to obtain steady state solutions which are independent of the time step. In the previous equation, a is the speed of sound.

3.2. Time Integration

The integration in time of Eq. (11) can be written using a 5-stage Runge-Kutta type scheme (Jameson *et al.*, 1981, and Jameson and Mavriplis, 1986) as

$$\begin{aligned} Q_i^{(0)} &= Q_i^n \ , \\ Q_i^{(\ell)} &= Q_i^{(0)} - \frac{\alpha_\ell \, \Delta t_i}{V_i} \left[C\left(Q_i^{(\ell-1)}\right) - V\left(Q_i^{(\ell-1)}\right) - D\left(Q_i^{\left(\ell'\right)}\right) \right] \qquad \ell = 1, \cdots, 5 \quad , \\ Q_i^{n+1} &= Q_i^{(5)} \ . \end{aligned} \tag{18}$$

In the previous equations, $C(Q_i)$, $V(Q_i)$ and $D(Q_i)$ are, respectively, the convective operator, the viscous operator and the artificial dissipation operator calculated for the i-th control volume. These operators are calculated according to the spatial discretisation scheme and they were detailed in the previous section. The α_ℓ coefficients are 1/4, 1/6, 3/8, 1/2 and 1 for $\ell = 1, \cdots, 5$, respectively. The ℓ' superscript indicates that the artificial dissipation operator is calculated only on the first, third and fifth stages. For the inviscid calculations, the artificial dissipation operator is calculated in the first and in the second stages.

The time step for each volume, Δt_i, is calculated using the CFL number. Hence,

$$\Delta t_i = \frac{\text{CFL} \ \ell_i}{(|\vec{q}_i| + a_i)} \ , \tag{19}$$

where a_i is the speed of sound in the i-th element, $|\vec{q}_i|$ is the magnitude of the flow velocity in the i-th element and ℓ_i is the characteristic length of the element. The characteristic length was set as the smallest distance between the element centroid and the centroids of each face that forms the element.

3.3. Boundary Conditions and Adaptive Mesh Refinement

"Ghost" volumes were used in order to enforce the boundary conditions. The boundary conditions for external flow implemented in the 3-D finite volume code were wall, for viscous and inviscid flows, farfield, symmetry and supersonic exit conditions. A detailed discussion of the boundary conditions considered for the present numerical tool can be found in Scalabrin (2002).

The quality of the numerical simulations is extremely dependent on the mesh. For a good numerical solution, it is necessary to have points concentrated in the regions where the flow presents sudden variations. The idea behind the adaptive mesh refinement is to attribute to the flow the responsibility of concentrating computational points by using automatic routines that alter the mesh. In this work, the option of adding points where necessary has been chosen because of the ease of implementation in an unstructured grid context. Furthermore, the adaptation algorithm implemented allows for the existence of hanging nodes in the mesh. The treatment of the resulting hanging nodes is a very important aspect of the code, but it has a very simple implementation. The sensor for regions that need refinement uses an undivided density gradient, normalised by the largest difference in density verified in the flow, i.e.,

$$(\text{sensor})_i = \frac{\sum_{m=1}^{nb} |\rho_m - \rho_i|}{|\rho_{\max} - \rho_{\min}|_{\ i}} \ . \tag{20}$$

If this sensor is greater than a threshold value, the volume is refined. The interested reader is referred to Scalabrin (2002) for more details on the adaptive mesh refinement algorithm.

4. Turbulence Modelling

Two turbulence closures have been chosen in the present context, namely, the Spalart-Allmaras (SA) single-equation model and the Menter SST two-equation model. Both closures are particularly suited for aerodynamic flow simulations and separation prediction. Furthermore, they are also less restrictive with respect to the grid refinement near the wall than two-equation models such as the $k-\epsilon$ family of models.

Both models are solved according to the finite volume approach. The convective term is discretized using a simplified first-order upwind scheme and the diffusion term is discretized using a centred scheme. The time march is performed using the implicit Euler scheme. One should observe that the use of an implicit scheme for the time march, in an unstructured mesh, leads to a sparse linear system. The solution for this system of equations is obtained using the biconjugate gradient method. More details of the implementation can be found in Scalabrin (2002).

4.1. SA Model

The Spalart-Allmaras single-equation model (Spalart and Allmaras, 1994), already written for a compressible flow, is given in its dimensionless form by

$$\frac{\partial \tilde{\mu}}{\partial t} = \underbrace{c_{b1}\tilde{S}\tilde{\mu}}_{P(\tilde{\mu})} - \underbrace{\frac{M_\infty}{Re}c_{w1}f_w\rho\left(\frac{\tilde{\nu}}{d}\right)^2}_{S(\tilde{\mu})} - \underbrace{\nabla\cdot(\tilde{\mu}\vec{u})}_{C(\tilde{\mu})} + \frac{M_\infty}{Re}\frac{1}{\sigma}\left\{\underbrace{\nabla\cdot[(\mu_\ell+\tilde{\mu})\nabla\tilde{\nu}]}_{D_1(\tilde{\mu})} + \underbrace{c_{b2}\,\rho\,\nabla\tilde{\nu}\cdot\nabla\tilde{\nu}}_{D_2(\tilde{\mu})}\right\} . \tag{21}$$

The variable solved for by this equation, $\tilde{\mu}$, is defined as $\tilde{\mu}=\rho\tilde{\nu}$ and the variable $\tilde{\nu}$ relates to the kinematic eddy viscosity by

$$\nu_t = \tilde{\nu}f_{v1} , \qquad f_{v1} = \frac{\chi^3}{\chi^3 + {c_{v1}}^3} , \qquad \chi = \frac{\tilde{\nu}}{\nu_\ell} . \tag{22}$$

The production term, $\tilde{S}$, is given by

$$\tilde{S} = S + \frac{1}{Re}\frac{\tilde{\nu}}{\kappa^2 d^2}f_{v2} , \qquad f_{v2} = 1 - \frac{\chi}{1+\chi f_{v1}} , \tag{23}$$

where S is the magnitude of the vorticity vector

$$S = \sqrt{2\Omega_{ij}\Omega_{ij}} , \qquad \Omega_{ij} = \frac{1}{2}\left(\frac{\partial u_i}{\partial x_j} - \frac{\partial u_j}{\partial x_i}\right) . \tag{24}$$

Variable d represents the distance to the closest wall. The wall damping function, f_w, is defined as

$$f_w = g\left(\frac{1+{c_{w3}}^6}{g^6+{c_{w3}}^6}\right)^{\frac{1}{6}} , \qquad g = r + c_{w2}\left(r^6 - r\right) , \qquad r = \frac{M_\infty}{Re}\frac{\tilde{\nu}}{\tilde{S}\kappa^2 d^2} . \tag{25}$$

The model constants are obtained from the calibration of the model for classical turbulent flows. Hence, these constants can be written as

$$c_{b1} = 0.1355 , \quad c_{b2} = 0.622 , \quad c_{v1} = 7.1 , \quad \sigma = \frac{2}{3} , \quad \kappa = 0.41 ,$$
$$c_{w1} = \frac{c_{b1}}{\kappa} + \frac{(1+c_{b2})}{\sigma} , \quad c_{w2} = 0.3 , \quad c_{w3} = 2 . \tag{26}$$

This same model has been applied without any further modification by the CFD community for 3-D compressible flows with good results (Menter and Grotjans, 2000).

The spatial discretisation of Eq. (21) is obtained by an integration of this equation in a finite volume. If one applies the usual mean property definition for a finite volume scheme and the Gauss theorem to the SA model transport equation, one obtains

$$\frac{\partial \tilde{\mu}_i}{\partial t} + \frac{1}{V_i}\int_{S_i}\vec{u}\,\tilde{\mu}\cdot d\vec{S} - \frac{M_\infty}{Re\,\sigma}\frac{1}{V_i}\int_{S_i}[(\mu_\ell+\tilde{\mu})\,\nabla\tilde{\nu}]\cdot d\vec{S} - \frac{c_{b2}M_\infty}{Re\,\sigma}\rho_i\,\nabla\tilde{\nu}_i\cdot\nabla\tilde{\nu}_i - (P(\tilde{\mu}_i) - S(\tilde{\mu}_i)) = 0 , \tag{27}$$

and one should note that the last three terms in the left-hand side of this equation, namely, $P(\tilde{\mu})$, $S(\tilde{\mu})$ and $D_2(\tilde{\mu})$, have been considered constant in the i-th volume. The surface integrals can be substituted by summations over the faces that form the i-th volume, which results in

$$\frac{\partial \tilde{\mu}_i}{\partial t} + \frac{1}{V_i}\sum_{k=1}^{nf}\vec{u}\,\tilde{\mu}\cdot\vec{S}_k - \frac{1}{V_i}\frac{M_\infty}{Re\,\sigma}\sum_{k=1}^{nf}[(\mu_\ell+\tilde{\mu})\,\nabla\tilde{\nu}]\cdot\vec{S}_k - \frac{c_{b2}M_\infty}{Re\,\sigma}\rho_i\,\nabla\tilde{\nu}_i\cdot\nabla\tilde{\nu}_i - (P(\tilde{\mu}_i) - S(\tilde{\mu}_i)) = 0 . \tag{28}$$

This approach is very straightforward and easy to implement. The modified eddy viscosity at the farfield boundary, as well as its initial value, are set to $\tilde{\nu}_\infty = 0.0001$. The wall boundary condition is $\tilde{\nu}_{wall} = 0$. Zero-th order extrapolation is performed at other boundaries.

4.2. SST Model

For the two-equation model used in the present work, the first equation solves for the turbulent kinetic energy, k, which is nondimensionalised by a_∞^2/Re. The second equation solves for a time-scale variable, ω, which is nondimensionalised by a_∞/d. For the model formulation, which is presented in the forthcoming paragraphs, the Einstein indicial notation is being used.

The Menter SST model is derived from both the original $k-\omega$ (Menter, 1993) and the standard $k-\epsilon$ (Menter, 1994) models. It solves some reported problems of the $k-\omega$ closure regarding freestream value dependency while keeping the better numerical behaviour of this model at low-Reynolds number regions when compared to standard $k-\epsilon$ closures. The SST closure, written for a compressible flow, can be given in its dimensionless form as

$$\frac{\partial \overline{k}}{\partial t} = P - \beta^* \rho \omega k - \frac{\partial}{\partial x_j}\left(\overline{k} u_j\right) + \frac{M_\infty}{Re}\frac{\partial}{\partial x_i}\left[\left(\mu_\ell + \sigma_k \mu_t\right)\frac{\partial k}{\partial x_i}\right] , \tag{29}$$

$$\frac{\partial \overline{\omega}}{\partial t} = \frac{\gamma_t}{\nu_t} P - \beta \rho \omega^2 - \frac{\partial}{\partial x_j}\left(\overline{\omega} u_j\right) + \frac{M_\infty}{Re}\frac{\partial}{\partial x_i}\left[\left(\mu_\ell + \sigma_\omega \mu_t\right)\frac{\partial \omega}{\partial x_i}\right] + \frac{M_\infty}{Re}\underbrace{2\left(1-F_1\right)\rho\sigma_{\omega 2}\frac{1}{\omega}\frac{\partial k}{\partial x_i}\frac{\partial \omega}{\partial x_i}}_{CD} . \tag{30}$$

The new term that appears underbraced in the ω equation comes from the original $k-\epsilon$ equation rewritten in terms of variable ω, where $\epsilon = \beta^* k\omega$. This term represents a cross diffusion term of the turbulence variables and it is turned on outside the viscous layers. The turbulent variables solved for by this set of transport equations are given by $\overline{k} = \rho k$ and $\overline{\omega} = \rho\omega$ where k is the dimensionless turbulent kinetic energy and ω is the dimensionless turbulent dissipation. The production term, P, is given by

$$P = \mu_t\left[\left(\frac{\partial u_i}{\partial x_j} + \frac{\partial u_j}{\partial x_i}\right)\frac{\partial u_i}{\partial x_j} - \frac{2}{3}\left(\frac{\partial u_m}{\partial x_m}\right)^2\right] - \frac{2}{3}\rho\, k\, \frac{\partial u_m}{\partial x_m} . \tag{31}$$

The F_1 variable is a blending function that turns on the $k-\omega$ closure in low-Reynolds number regions and the standard $k-\epsilon$ outside boundary layers. It is defined as

$$F_1 = tanh\left(arg_1^4\right) , \qquad arg_1 = \min\left[\max\left(\frac{\sqrt{\frac{M_\infty k}{Re}}}{0.09\omega d} \;,\; \frac{500 M_\infty \nu_\ell}{Re\omega d^2}\right), \frac{4\rho\sigma_{\omega 2} k}{CD_{k\omega} d^2}\right] , \tag{32}$$

where

$$CD_{k\omega} = \max\left(2\rho\sigma_{\omega 2}\frac{1}{\omega}\frac{\partial k}{\partial x_j}\frac{\partial \omega}{\partial x_j}, 10^{-10}\right) . \tag{33}$$

Model constants are generally calculated as

$$\phi = F_1\phi_1 + (1-F_1)\phi_2 , \tag{34}$$

where ϕ_1 represents the set of constants for the $k-\omega$ model and ϕ_2 the set for the standard $k-\epsilon$ model. The following sets are used

$$\sigma_{k1} = 0.5 \;,\; \sigma_{\omega 1} = 0.5 \;,\; \beta_1 = 0.075 \;,\; \beta^* = 0.09 \;,\; \kappa = 0.41 \;,\; \gamma_{t1} = \frac{\beta_1}{\beta^*} - \frac{\sigma_{\omega 1}\kappa^2}{\sqrt{\beta^*}} , \tag{35}$$

$$\sigma_{k2} = 1.0 \;,\; \sigma_{\omega 2} = 0.855 \;,\; \beta_2 = 0.0828 \;,\; \beta^* = 0.09 \;,\; \gamma_{t2} = \frac{\beta_2}{\beta^*} - \frac{\sigma_{\omega 2}\kappa^2}{\sqrt{\beta^*}} . \tag{36}$$

It is known in the CFD community that standard two-equation models are not capable of accurately computing strong adverse pressure gradient flows with separation. These models require a stronger pressure gradient or a longer running length to separate than indicated by experiments. It is demonstrated that this is a result of the missing effect of turbulent shear-stress transport. In order to take this shear-stress into account, the eddy viscosity expression is modified for the SST model, which results in

$$\nu_t = \frac{a_1 k}{\max\left(a_1\omega, F_2\Omega\right)} , \tag{37}$$

inside boundary layers, where Ω is a measure of the strain rate in this viscous layer and usually the absolute value of vorticity is used. The F_2 variable is another blending function that turns this new definition on inside boundary layers. This is defined as

$$F_2 = \tanh\left(arg_2^2\right) , \qquad arg_2 = \max\left(2\frac{\sqrt{\frac{M_\infty k}{Re}}}{0.09\omega d}, \frac{500 M_\infty \nu_\ell}{Re\omega d^2}\right) . \tag{38}$$

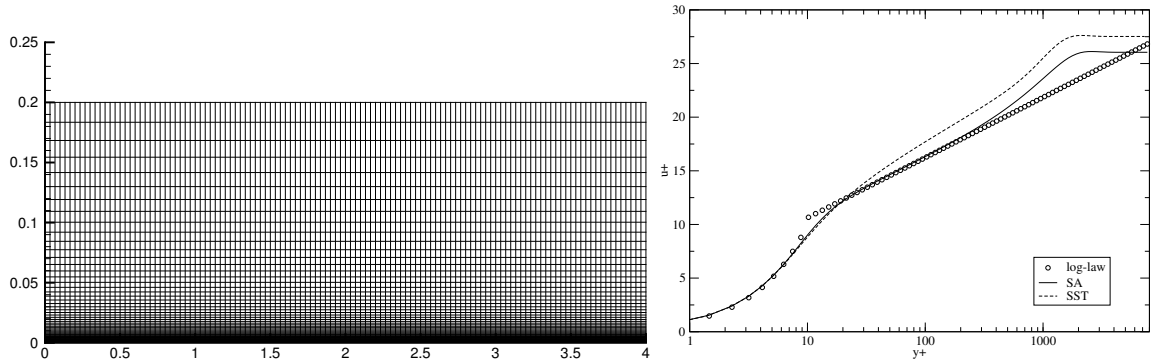

(a) Computational mesh.

(b) Boundary layers.

Figure 1: Numerical results for a $M_\infty = 0.3$ flat plate flow.

The discretisation of the production, destruction, advection and diffusion terms in Eqs. 29 and 30 are very similar to what has already been discussed for the SA model. The discretisation in a finite volume of the cross-diffusion term, CD, underbraced in Eq. 30, is performed considering this term constant in the i-th volume in a very similar fashion to what is done to the D_2 term for the SA model. Therefore, if one integrates Eq. 30 in a finite volume and one considers the mean property definition for a finite volume, one obtains the discretisation of the cross-diffusion term as

$$\int_{V_i} CD_i \, dV = 2 \, V_i \, \sigma_{\omega 2} \, (1 - F_1)_i \, \rho_i \frac{1}{\omega_i} \nabla k_i \cdot \nabla \omega_i \ . \tag{39}$$

The following set of freestream conditions is chosen

$$\omega_\infty = 10 \frac{M_\infty}{L} \ , \ \nu_{t\infty} = 10^{-3} \nu_\infty \ , \ k_\infty = \frac{M_\infty}{Re} \nu_{t\infty} \omega_\infty \ , \tag{40}$$

where L is the approximate length of the computational domain. Wall boundary conditions considered are

$$k = 0 \ , \quad \omega = 60 \frac{M_\infty}{Re} \frac{\nu}{\beta_1 (\Delta y_1)^2} \ , \tag{41}$$

where Δy_1 is the distance to the wall of the closest point away from it. Zero-th order extrapolation is performed at other boundaries.

5. Results and Discussion

In the present section, turbulent flow simulation results obtained with the turbulence models implemented are presented. Various geometries and flow conditions are considered in the present effort. Subsonic flows over a zero-pressure gradient flat plate are considered in order to assess the correctness of the implementation. A theoretical solution for the turbulent boundary layer that builds up over the flat plate is available and the numerical results are compared to such data. Furthermore, transonic and supersonic turbulent flows about typical aerospace configurations are also considered in the present analysis.

The flat plate turbulent flow is a very important test case since a theoretical solution is provided for the turbulent boundary layer that builds up over the surface, known as the log-law solution (Bigarella, 2002). The flow conditions considered are Mach number $M_\infty = 0.3$, zero angle of attack, and Reynolds number $Re = 1.0$ million. Simulations with both the SA and the SST turbulence models are included in order to assess the behaviour of these models. The mesh about the flat plate is clustered near the flat plate surface and leading edge in order to account for the larger velocity gradients that are expected in these regions. A 2-D view of the 3-D hexahedral mesh is presented in Fig. 1. Figure 1 also shows the turbulent numerical boundary layers compared to the theoretical log-law solution. The definition of the dimensionless $u+$ and $y+$ variables in this figure are

$$y^+ = y \frac{Re}{\nu} u^* \ , \qquad u^+ = \frac{u}{u^*} \ , \qquad u^* = \sqrt{\frac{\nu}{Re} \left| \frac{\partial u}{\partial y} \right|} \ . \tag{42}$$

In the previous equation, only the most important portion of the viscous stress tensor has been considered to compute the wall shear stress. A strikingly coherence between the SA model result and the theoretical curve can be observed in Fig. 1. In the case of the SST closure, the coherence between both results is not as good

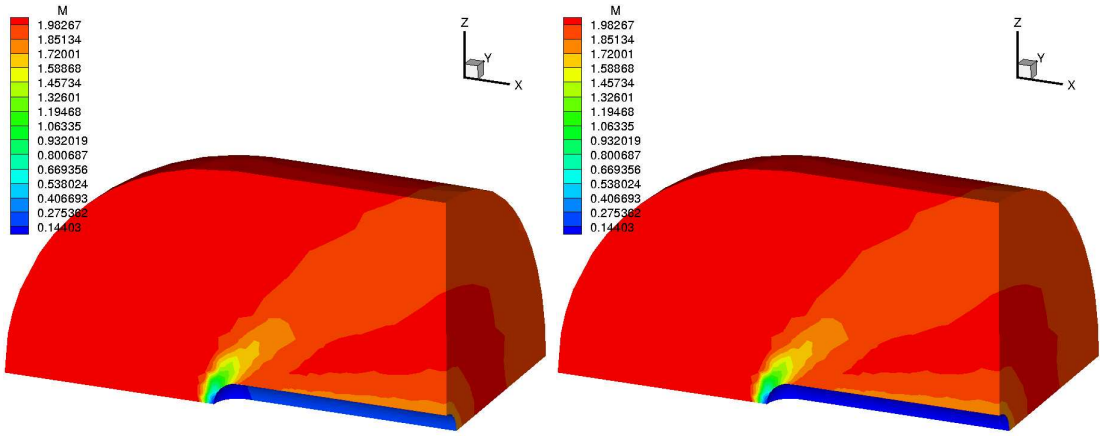

(a) SA model. (b) SST model.

Figure 2: Mach number contours over the hemisphere-cylinder at $M_\infty = 2.0$ and $\alpha = 0$ deg. Reynolds number is $Re = 4.4$ million.

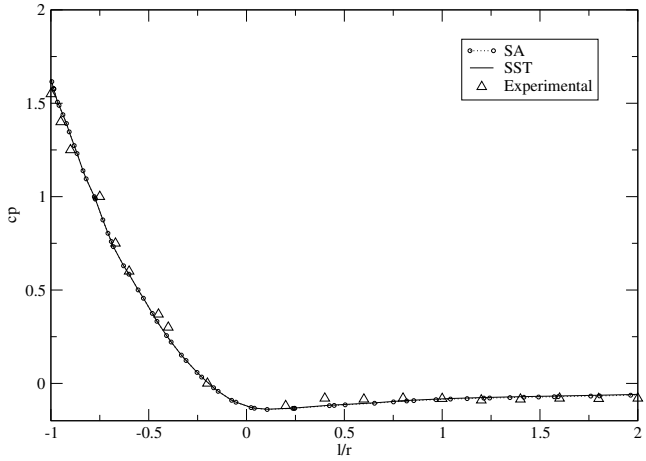

Figure 3: Pressure coefficient distributions over the hemisphere-cylinder wall obtained experimentally and numerically with the SST and the SA models.

in the inertial portion of the boundary layer. A very similar behaviour of the SST closure in this test case has been observed in a finite difference context (Bigarella, 2002). This may be indicative of some issues concerning the formulation provided in the articles available to the authors to guide the model implementation, especially regarding the model constants. Due to better numerical results and lower computational cost, the SA model has been chosen for the forthcoming VLS simulations.

Simulations of supersonic flows over an hemisphere-cylinder body were performed with freestream Mach number $M_\infty = 2.0$, zero angle of attack and Reynolds number $Re = 4.4$ million. In these simulations, both the SA and SST turbulence models are exercised, as a form of comparing their results. In Fig. 2, one can observe the Mach number contours over the hemisphere-cylinder obtained in the present calculations for both closures.

One can observe in Fig. 2 that the numerical results obtained with the turbulence modelling capability are qualitatively good. Both turbulence models capture well the position of the detached shock wave near the vehicle nose, as well as the expansion waves along the hemisphere region of the configuration. A quantitative comparison is available in Fig. 3. In this figure, numerical results are compared to experimental data regarding pressure coefficient, Cp, distributions. One can observe in this figure that the numerical distributions compare very well with the experimental data, which is a clear indication of the good quality of the results that can be obtained with the present numerical tool.

The supersonic turbulent flow over the VLS at $M_\infty = 2.0$, $Re = 30$ million and 2 deg. angle of attack has been simulated. The mesh used in this case has 100,815 nodes and 89,280 elements. Due to the previously mentioned reasons, the SA model has been used in the simulations. In Fig. 4, Mach number contours over the VLS forebody are presented. One can observe in this figure that the bow shock in the windside is stronger than in the leeside because the deflection in the flow is larger. Furthermore, the boundary layer on the leeside

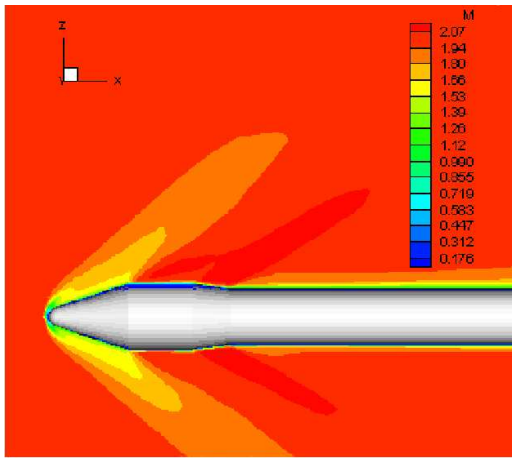

(a) Mach number contours.

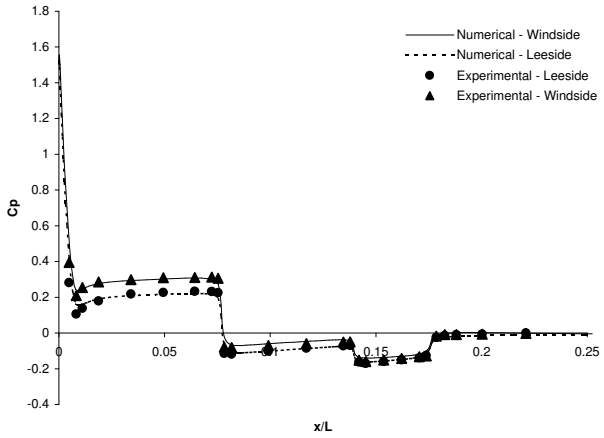

(b) Cp distributions.

Figure 4: Turbulent flow results for the VLS second stage flight configuration at $M_\infty = 2.0$, $Re = 25$ million and $\alpha = 2$ deg.

is thicker than on the windside. A comparison between numerical and experimental Cp distributions on the vehicle forebody is presented in Fig. 4. The numerical solution for the leeside presents good agreement with the numerical data. The solution for the windside, however, indicates slightly higher pressures over the payload fairing and boattail regions than the experimental results. Nevertheless, the results for the windside captured the main tendencies of the pressure coefficient distribution.

Figure 5 presents Mach number contours over the VLS forebody at $M_\infty = 0.9$, $Re = 25$ million and zero angle of attack. One can observe in this figure that a supersonic expansion occurs over the end of the conical forebody. This causes the formation of a supersonic region over the payload cylinder which is ended by a shock wave. Due to the boundary layer, this shock wave does not reach the body. The region after the shock wave presents very small velocities, but the boundary layer does not separate because of the turbulent characteristics of the flow. In fact, laminar simulations of this flow condition indicate boundary layer separation. A comparison between pressure coefficient distributions on the VLS surface for the Euler and the turbulent numerical solutions, as well experimental data, is shown in Fig. 5. The simulations considering turbulence effects clearly do a better job if compared with the Euler simulation for this case. A much better solution is obtained, which captures the shock wave over the payload fairing and which correctly predicts the position of the compression peak at the end of the boattail.

6. Concluding Remarks

A computational code which solves the 3-D, compressible RANS equations is presented. An explicit Runge-Kutta scheme to march the governing equations in time is used. The fluxes on the volume faces are computed by a centred scheme plus explicitly added artificial dissipation to control non-linear instabilities of the formulation. The code is designed to use unstructured meshes composed by any combination of tetrahedra, hexahedra, prisms and pyramids and it has implemented adaptive mesh refinement routines in order to improve the solution quality. Turbulence effects are added to the formulation by turbulence models. The Spalart-Allmaras single-equation and the SST two-equation turbulence closures have been chosen. The comparison of the numerical boundary layers over a zero-pressure gradient flat plate flow with the corresponding theoretical log-law solution showed the level of accuracy that can be obtained with the present formulation. Furthermore, the code is also able to correctly solve for more complex flows, such as transonic or supersonic turbulent flows about typical aerospace configurations. Again, good approximation between experimental and numerical results could be obtained for such cases. The results presented here are a good indication of the capability of simulating turbulent flows about realistic aerospace configurations that has been developed by the CFD group at IAE.

7. Acknowledgements

The present work was partially supported by Conselho Nacional de Desenvolvimento Científico e Tecnológico, CNPq, under the Integrated Project Research Grant No. 522.413/ 96-0. The authors also acknowledge CESUP, at Universidade Federal do Rio Grande do Sul, for providing the necessary computational resources to address some of the simulations presented in this work.

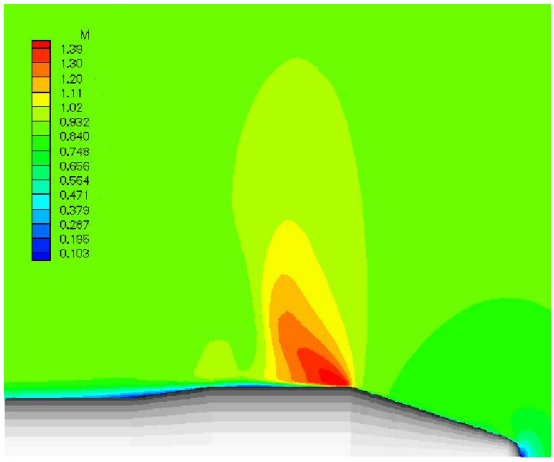

(a) Mach number contours.

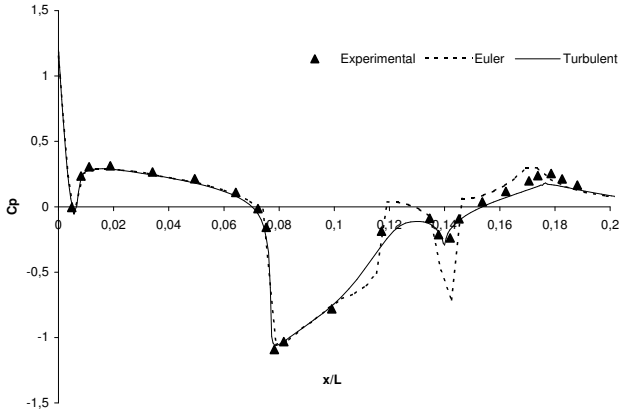

(b) Cp distributions.

Figure 5: Turbulent flow results for the VLS second stage flight configuration at $M_\infty = 0.9$, $Re = 25$ million and zero angle of attack.

8. References

Azevedo, J.L.F., Moraes, P., Jr., Maliska, C.R., Marchi, C.H., and Silva, A.F.C., 1996, "Code Validation for High-Speed Flow Simulation over Satellite Launch Vehicle," Journal of Spacecraft and Rockets, Vol. 33, No. 1, pp. 15-21.

Bigarella, E.D.V., 2002, "Three-Dimensional Turbulent Flow Simulations over Aerospace Configurations," Master Thesis, Instituto Tecnológico de Aeronáutica, São José dos Campos, SP, Brazil.

Bigarelli, E.D.V., Mello, O.A.F., and Azevedo, J.L.F., 1999, "Three Dimensional Flow Simulations for Typical Launch Vehicles at Angle of Attack," Proceedings of the 15th Brazilian Congress of Mechanical Engineering – COBEM 99, Águas de Lindóia, SP, Brazil (publication in CD-ROM without page numbering).

Buonomo, C.A., and Azevedo, J.L.F., 1997, "Transonic Turbulent Flow Simulations over the VLS Forebody," Proceedings of the 14th Brazilian Congress of Mechanical Engineering – COBEM 97, Bauru, SP, Brazil (publication in CD-ROM without page numbering).

Jameson, A., and Mavriplis, D., 1986, "Finite Volume Solution of the Two-Dimensional Euler Equations on a Regular Triangular Mesh," AIAA Journal, Vol. 24, No. 4, pp. 611-618.

Jameson, A., Schmidt, W., and Turkel, E., 1981, "Numerical Solution of the Euler Equations by Finite Volume Methods Using Runge-Kutta Time-Stepping Schemes," AIAA Paper No. 81-1259, AIAA 14th Fluid and Plasma Dynamics Conference, Palo Alto, CA, USA.

Mavriplis, D.J., 1990, "Accurate Multigrid Solution of the Euler Equations on Unstructured and Adaptive Meshes," AIAA Journal, Vol. 28, No. 2, pp. 213–221.

Menter, F.R., 1993, "Zonal Two Equation $k - \omega$ Turbulence Models for Aerodynamic Flows," AIAA Paper No. 93-2906, AIAA 24th Fluid Dynamics Conference, Orlando, FL, USA.

Menter, F.R., 1994, "Two-Equation Eddy-Viscosity Turbulence Models for Engineering Applications," AIAA Journal, Vol. 32, No. 8, pp. 1598-1605.

Menter, F.R., and Grotjans, H., 2000, "Application of Advanced Turbulence Models to Complex Industrial Flows," Advances in Fluid Mechanics, Calculation of Complex Turbulent Flows, ed. G. Tzabiras, Southampton, UK.

Scalabrin, L.C., 2002, "Numerical Simulation of Three-Dimensional Flows over Aerospace Configurations," Master Thesis, Instituto Tecnológico de Aeronáutica, São José dos Campos, SP, Brazil.

Spalart, P.R., and Allmaras, S.R., 1994, "A One-Equation Turbulence Model for Aerodynamic Flow," La Recherche Aeropastiale Journal, Vol. 1, pp. 5-21.

Zdravistch, F., and Azevedo, J.L.F., 1990, "Numerical Simulation of High Speed Flows over Complex Satellite Launchers," Proceedings of the 3rd Brazilian Congress of Engineering and Thermal Sciences (ENCIT), Itapema, Santa Catarina, Brazil, pp. 233-238.